International Journal of ISSI, Vol.5 (2008), No. 2, pp. 1-7

# Using Finite Point Method for the Numerical Simulation of Heat Transfer Coupled with Microsegregation during Continuous Casting

M. Alizadeh[1*], S. A. Jenabali Jahromi[2]

*1-Department of Materials Science and Engineering, International Center for Science, High Technology & Environmental Sciences, Kerman, Iran*

*2- Department of Materials Science and Engineering, Shiraz University, Shiraz, Iran*

## Abstract

In the present work, a meshless method called Finite Point Method (FPM) is developed to simulate the solidification process of a continuously cast steel bloom in both primary and secondary cooling regions. The method is based on the use of a weighted least-square interpolation procedure. A transverse slice of the bloom moving at casting speed is considered as the computational domain and two dimensional heat transfer equations are solved in the computational domain. The present FPM-thermal analysis is coupled with the microsegregation model and used to investigate the capability of the FPM for use in hot tearing study. This hypothesis is verified by comparing surface temperatures simulated by both FPM (the method proposed in this study) and finite volume method (FVM) (the conventional method). Also the simulated surface temperatures are compared with thermography measurements. The results reveal that the proposed FPM can be used successfully both for the simulation of steel bloom to determine its temperature field and for hot tearing study.

*Keywords:* Numerical, Simulation, Continuous casting, Meshless, Finite Point, Solidification.

## 1- Introduction

Continuous casting has become the primary method for producing steel blooms, slabs, and billets. Quality control in continuous casting is the basis not only for reducing production costs and processing time but also for ensuring reproducibility of the casting operation and increased production [1)]. These can only be achieved if the thickness of the solidified shell and the temperature distribution along different cooling zones are known as two initial parameters of solidification in the continuous casting process [2-4)]. Calculating the values for these two parameters forms the first step in solidification control. For this purpose, solidification is simulated by solving the heat transfer equation, which is then used to calculate the thickness of the solidified shell and the strand temperature profile [5-8)]. The idea of using simulation to calculate and control solidification parameters is not merely a theoretical speculation but its practicality has already been demonstrated.

The methods commonly used for solidification simulation are FEM, FVM, and finite difference method (FDM). These methods are mesh-based in which the spatial domain where the partial differential governing equations are defined is often discretized into meshes. The basic principle underlying the formulation of these conventional numerical methods is that a mesh must be predefined to provide a certain relationship between the nodes [9)].

Meshless methods use a set of nodes scattered within the problem domain and on the boundaries of the domain to represent the problem domain and its boundaries. These sets of scattered nodes do not form a mesh, which means that no information on the relationship between the nodes is required at least for field variable interpolation.

Generally, mesh generation is not very easy, especially in a complex geometry (in the FEM) while the complex boundary conditions also cause difficulties for FDM. Despite some apparent similarities between FPM and FEM, a comparison of them for two dimensional problems reveals the advantages and superiority of FPM over FEM in certain respects. Generally speaking, it would be possible to summarize the advantages of the FPM as follows: (1) The manual work for data preparation is reduced because of the meshless feature; (2) The dependent variables and their gradients are continuous in the entire domain; (3) By modifying or refining the nodal distribution in FPM , a node can be easily moved, removed, or added in the domain, while a local mesh modification and the corresponding nodal and element renumbering will be necessary in FEM; (4) It would be possible to couple the thermo-mechanical calculations to the thermal analysis easily (especially, when compared

* *Corresponding author:*
*Tel: +98-342-6226611 Fax: +98-342-6226617*
*E-mail: alizadeh@icst.ac.ir*
*Address: Department of Materials Science and Engineering, International Center for Science, High Technology & Environmental Sciences, Kerman, Iran*

1. Assistant Professor
2. Professor

with FVM) [9-13]. Hence, FPM is gaining wider industrial applications.

Zhang et al [13] used FPM for the first time for modeling solidification in the continuous casting process. They simulated the solidification of a strand in the only mold region with a constant heat flux as boundary conditions. Their goal was to show that FPM can be applied for thermal analysis of the continuous casting process. Although they succeeded in achieving this objective, it is not yet clear whether FPM can be applied for other strand sizes (bloom or billet), if this technique could be used for the secondary cooling zone with complex boundary conditions, or if it can be coupled with microsegregation model and strain analysis.

The present work intends to develop an FPM for a 230×250 mm bloom for the mold, spray cooling, and radiation cooling regions. It will be shown that FPM could be used for complex boundary conditions (in the mold and below the mold) and also employed to calculate the temperature profile as well as the solidified shell thickness. Moreover, the FPM developed will be coupled with the microsegregation model and the strain model to analyze the mushy zone as well as the cracking strain. Variation of casting speed is investigated as an important factor in the convergence of equations to show the flexibility of FPM in the field of continuous casting modeling. Additionally, this article aims to provide a simple description of the basic principles of FPM.

## 2- Simulation by FPM

The first step in FPM is to provide the problem domain using sets of nodes scattered in the problem domain and its boundary. Figure 1 depicts a typical domain and the scattered nodes.

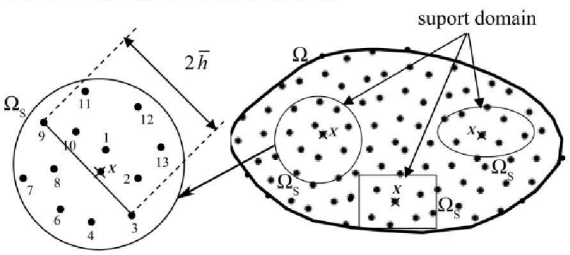


*Fig. 1. A typical problem domain, $\Omega$, represented by scattered nodes and three different shapes of support domains, $\Omega_s$, and the characteristic length defined in the support domain.*

Let us suppose we wanted to find an unknown function $u(X)$ (the field variable at any point of interest $X$). FPM is used to solve the equation system by interpolation of the unknown function within a small local domain, which is taken to be a circle centered at a point $X$ (see Figure 1). However, the small local domain can have different shapes and its dimension and shape can be different for different points of interest $X$, as shown in Figure 1. A support domain of a point $X$ determines the number of nodes to be used to support or approximate the function value at $X$; hence, it is termed the support domain of $X$ [9].

Generally, the field variable of $u(X)$ in FPM is approximated at any point of interest $X$ as follows:

$$u(X) = \sum_{k=1}^{n} \phi_k(X) u_k = \boldsymbol{\phi}^{\mathrm{T}} \boldsymbol{u} \qquad (1)$$

Here, $X$ is an arbitrary point in the problem domain with a circular support domain (e.g. $X = [x\ y]^{\mathrm{T}}$ in 2D and $X = [x\ y\ z]^{\mathrm{T}}$ in the 3D case). The term n is the number of nodes lying in the support domain of $X$, $u_k$ is the nodal field variable at the k-th node in the support domain, $\boldsymbol{u}$ is the vector of elements $u_k$, and $\phi_k(X)$ is the *k-th* element of the shape function vector $\boldsymbol{\phi}$ (which corresponds to the k-th node of the support domain) [9].

### 2-1- Shape function cteation

Creating the shape functions is the most important issue in FPM methods. The challenge is how to create the shape functions using only nodes scattered arbitrarily in a domain without any predefined mesh to provide connectivity of the nodes. A series of methods are proposed to construct the shape functions [9]. In this work, the moving least square (MLS) approach is used to construct the shape function. MLS method first approximates the field function by:

$$u^h(X) = \sum_{j=1}^{m} p_j(X) a_j(X) = \boldsymbol{p}^{\mathrm{T}}(X)\, \boldsymbol{a}(X) \qquad (2)$$

where, $p_j(X)$ is the $j$-th component of the vector $\boldsymbol{p}(X)$ which is termed "base interpolating function" and contains $m$ monomial basis functions. For a 2D problem,

$$\boldsymbol{p}(X) = [1 \quad x \quad y]^{\mathrm{T}} \quad \text{for m= 3} \qquad (3)$$

and

$$\boldsymbol{p}(X) = [1 \quad x \quad y \quad xy \quad x^2 \quad y^2]^{\mathrm{T}} \quad \text{for m= 6} \qquad (4)$$

Also in Equation 2, $\boldsymbol{a}(X)$ is the coefficient vector of elements $a_j(X)$. Therefore, the value of the variable function is approximated at a point like $X$ as a combination of values of the basic functions at that point, each weighted by $a_j$. All that needs to be done is to find suitable values for the coefficients $a_j$.

Let us assume that $X_1$, $X_2$, ....., $X_n$ are nodes located in the support domain of $X$ and that $u_1$, $u_2$, ....., $u_n$ are their corresponding nodal values. Figure 1 (left) depicts this support domain. Let us also suppose $X_k$ to be one of the domain nodes in the vicinity of point $X$. From Equation 2, $u_k$ can then be approximated using the value of $a$ at $X$:

$$u^h(X_k) = u_k = \boldsymbol{p}^{\mathrm{T}}(X_k)\boldsymbol{a}(X_k) \approx \boldsymbol{p}^{\mathrm{T}}(X_k)\boldsymbol{a}(X) \qquad (5)$$

For each node $k$ in the support domain, the squared error of Equation 5 can be written as a function of $X$:

$$E_k(X) = [\boldsymbol{p}^{\mathrm{T}}(X_k)\boldsymbol{a}(X) - u_k]^2 \qquad (6)$$

Apparently, $E_k(X)$ is expected to be smaller as $X$ gets closer to $X_k$. Thus, an appropriate formula for $\boldsymbol{a}(X)$ can be obtained by performing a minimization

task in which each of the error functions $E_k(X)$ is minimized to some degree considering the nearness of $X_k$ to $X$. For this purpose, the following function should be minimized:

$$J(X)=\sum_{k=1}^{n} W(X,X_k)E_k(X)=(\mathbf{P}^{\mathrm{T}}\boldsymbol{a}-\boldsymbol{u})^{\mathrm{T}}\mathbf{W}(\mathbf{P}^{\mathrm{T}}\boldsymbol{a}-\boldsymbol{u}) \quad (7)$$

where, $W(X,X_k)$ is called the weight function which should be chosen such that larger values are obtained when $X$ and $X_k$ are closer together. Here, we have chosen the exponential weight function as follows:

$$W(X,X_k)=\begin{cases} exp(-\dfrac{(X-X_k)^{\mathrm{T}}(X-X_k)}{\sigma^2} & \|X-X_k\|\le \mathrm{R} \\ 0 & \|X-X_k\|>\mathrm{R} \end{cases} \quad (8)$$

where, σ is a constant. The term R is the radius of the support domain. The matrices of **P**, ***u***, ***a***, and **W** are defined as:

$$\mathbf{P}=\begin{bmatrix} p(X_1) & p(X_2) & p(X_3) & \dots & p(X_{\mathrm{n}}) \end{bmatrix} \quad (9)$$

$$\boldsymbol{a}=\begin{bmatrix} a_1 & a_2 & a_3 & \dots & a_n \end{bmatrix}^{\mathrm{T}} \quad (10)$$

$$\boldsymbol{u}^{T}=\begin{bmatrix} u_1 & u_2 & u_3 & \dots & u_n \end{bmatrix} \quad (11)$$

$$\mathbf{W}=\begin{bmatrix} W(X,X_1) & & & & 0 \\ & W(X,X_2) & & & \\ & & \dots & & \\ & & & \dots & \\ 0 & & & & W(X,X_{\mathrm{n}}) \end{bmatrix} \quad (12)$$

In MLS approximation, at an arbitrary point $X$, $a(X)$ is chosen to minimize the weighted residual (Equation 7). The minimization condition requires:

$$\nabla_a J(X)=0 \quad (13)$$

$$\nabla_a J(X)=2\mathbf{P}\mathbf{W}(\mathbf{P}^{\mathrm{T}}\boldsymbol{a}-\boldsymbol{u})=0 \quad (14)$$

Equation 14 is rewritten as Equation 15:

$$\mathbf{P}\mathbf{W}\mathbf{P}^{\mathrm{T}}\boldsymbol{a}(X)=\mathbf{P}\mathbf{W}\boldsymbol{u} \quad (15)$$

To simplify the notation, let us define new matrices as follows:

$$\mathbf{A}=\mathbf{P}\mathbf{W}\mathbf{P}^{\mathrm{T}} \quad (16)$$

$$\mathbf{B}=\mathbf{P}\mathbf{W} \quad (17)$$

Therefore, the matrix of coefficients could be written as:

$$\boldsymbol{a}(X)=\mathbf{A}^{-1}\mathbf{B}\boldsymbol{u} \quad (18)$$

Considering Equations 2 and 8, it is possible to write the field function as follows:

$$u(X)\cong u^h(X)=\boldsymbol{p}^{\mathrm{T}}(X)\mathbf{A}^{-1}\mathbf{B}\boldsymbol{u}=\boldsymbol{\phi}^{\mathrm{T}}\boldsymbol{u} \quad (19)$$

where, the term ϕ is the shape function. Note that in this formulation only the shape function is a function of $X$. This is very useful because in solving the differential equation by FPM, the derivations are considered only on the shape function [10].

### 3- Solution of the governing equations by FPM

#### 3-1- Heat transfer model

FPM is applied to solve the energy equation with boundary conditions of the continuous casting of breakout bloom in various cooling areas. Figure 2 shows the problem domain of the bloom represented by a series of scattered nodes. The point step is 3 mm and 1680 points are distributed in the problem domain. In fact, Figure 2 depicts the transverse slice which is cooled in the boundaries across various cooling regions. We suppose this slice to be moving down at a velocity equal to the casting speed from the meniscus up to the end point of the simulation. This strategy aids us to consider a two-dimensional solution of the equations for the whole strand.

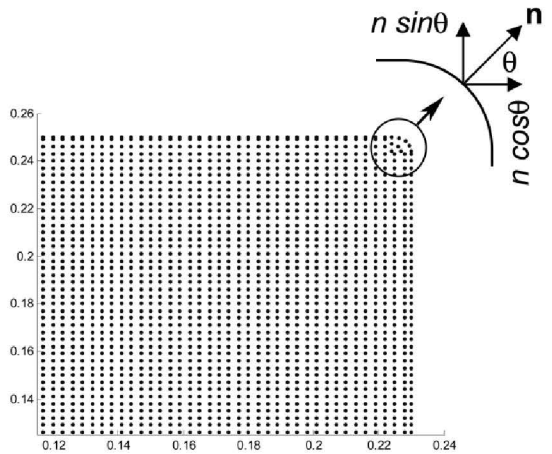


*Fig. 2. The problem domain represented by the nodes scattered in the domain and at the boundaries.*

Equation 20 (energy equation) is solved for the nodes located in the problem domain. Equation 21 is Neumann boundary conditions and is solved for the nodes located on the boundary. Finally, Equation 22 is Dirichlet boundary condition considered for all the nodes at time zero. For a convection-diffusion problem such as energy equation, a special treatment is needed to stabilize the numerical approximation [11].

$$\rho(\mathrm{T})C'(\mathrm{T})\frac{\partial \mathrm{T}}{\partial \mathrm{t}}=\mathrm{k}(\mathrm{T})\nabla^2\mathrm{T}=\mathrm{k}(\mathrm{T})\left[\frac{\partial^2 \mathrm{T}}{\partial \mathrm{x}^2}+\frac{\partial^2 \mathrm{T}}{\partial \mathrm{y}^2}\right] \quad (20)$$

$$-k(T)\frac{\partial T}{\partial n}=q_n \quad (21)$$

$$T=T_{pour} \quad for \quad t=0 \quad (22)$$

Onate et al stabilized the Neumann boundary using the "residual stabilization technique"[11]. They proposed Equation 23 as the stabilized Neumann boundary using the simple 1D convection-diffusion problem.

$$-k(T)\frac{\partial T}{\partial n}=q_n+\frac{h}{2}r \quad (23)$$

where

$$r=k(T)\nabla^2 T+Q_s=k(\mathrm{T})\frac{\partial^2 \mathrm{T}}{\partial x^2}+k(\mathrm{T})\frac{\partial^2 \mathrm{T}}{\partial y^2}+Q_s \quad (24)$$

The term $h$ is the characteristic length and can be found by using searching the exact nodal values for the simple 1D problem with $Q_s = 0$. Application of this concept to FPM by Onate et al gives

$$h = \begin{cases} \dfrac{\alpha \bar{h}}{4} & \text{for quadratic interpolations s} \\ \dfrac{\alpha \bar{h}}{2} & \text{for linear interpolations} \end{cases} \quad (25)$$

where, $\alpha$ is defined as a function of Peclet number as follows:

$$\alpha = \mathbf{coth}|Pe| - \frac{1}{|Pe|} \quad (26)$$

The term $\bar{h}$ is measured along the streamline between the end points for a particular support domain as shown in Figure 1.

As a first step, let us discretize the energy equation in the time space for any node $k$ in the support domain including the internal nodes (Equation 20) as follows:

$$\rho(T_k^t)\cdot C'(T_k^t)\cdot\frac{T_k^{t+\Delta t}-T_k^t}{\Delta t} = k(T_k^t)\cdot\left(\frac{\partial^2 T_k^t}{\partial x^2}+\frac{\partial^2 T_k^t}{\partial x^2}\right) \quad (27)$$

and for the support domain including the points lying on the boundaries (28)

$$-k(T_k^t)\left[n\sin\theta\cdot\frac{\partial T_k^t}{\partial x}+n\cos\theta\frac{\partial T_k^t}{\partial x}\right] = q_n + \frac{h}{2}\cdot\left[k(T_k^t)\cdot\left(\frac{\partial^2 T_k^t}{\partial x^2}+\frac{\partial^2 T_k^t}{\partial x^2}\right)\right]$$

Here, the term in the left hand bracket is $\partial T/\partial x$ for $\theta = 0$ and $\partial T/\partial y$ for $\theta = 90$; otherwise, it is related to $\partial T/\partial n$ at the corner of the problem domain (see Figure 2). In fact, the terms for unknown temperature and its derivatives presented in Equations 27 and 28 for any node k at time t are calculated by FPM as follows:

$$T_k^t \approx \phi^{\mathrm{T}}\, \boldsymbol{T}^t \quad (29)$$

$$\frac{\partial T_k^t}{\partial x} = \left(\frac{\partial \phi}{\partial x}\right)^{\mathrm{T}} \boldsymbol{T}^t \quad (30)$$

$$\frac{\partial^2 T_k^t}{\partial x^2} = \left(\frac{\partial^2 \phi}{\partial x^2}\right)^{\mathrm{T}} \boldsymbol{T}^t \quad (31)$$

To investigate the effect of liquid convection on thermal field, it is common to employ an effective thermal conductivity in the liquid zone [2, 14]. The effective thermal conductivity depends on such operational parameters as electromagnetic mold stirrer conditions, geometry and size of the submerged entry nozzle, and the amount of superheat. In the present model, Louhenkilpi et al's [14] simple suggestion was applied which requires an increase of two times for the conductivity of the liquid for a bloom with an electromagnetic stirrer in the mold region.

### 3-2- Boundary conditions for heat transfer

The local heat flux density ($q_n$) for every cooling section is calculated as follows:

In the mold region [15]:

$$q_n = \frac{\alpha\,\Delta T_w^T\,\rho_w\,C_w\,Q}{P_m}\times\frac{e^{-\alpha z}}{1-e^{-\alpha H_{me}}} \quad (32)$$

where, $Q$ is cooling water rate *($m^3/s$)*, $\rho_w$ is water density *(997 kg/ $m^3$ at 25°C)*, $C_w$ is the heat capacity of water *(4180 J $kg^{-1}$ at 25°C)*, $H_m$ is mold length *(m)*, $P_m$ is the perimeter of the tube mold (billet and bloom mold), $z$ is distance from meniscus *(m)*, $\alpha$ is the slope of straight lines in a *q-z* half-logarithmic plot (almost *1.5$m^{-1}$*), $\Delta T_w^T$ is the total increase of the cooling water temperature *(°C)*, and the term $H_{me}$ is the effective mold length in contact with the melt.

In the spray cooling region [3]:

$$q_n = h_j(T - T_w) \quad (33)$$

where, the subscript $j$ represents the number of spray cooling sections. In the present research, the spray cooling zone was divided into 3 sections according to the flow rate of water, i.e. foot roll, mobile section, and fixed section areas. $h_j$ is the convective heat transfer coefficient in the $j^{th}$ section, which can be calculated as follows:

$$h_j = h_{\alpha j}\,.\,w_j^r + h_{r\,j} \quad (34)$$

where, $h_{\alpha j}$, $r$ and, $h_{r\,j}$ are the parameters of the nozzle; for an air-mist spray nozzle, $h_{\alpha j}$ is *0.35*, $r$ is *0.556,* and $h_{r\,j}$ is *0.13*, respectively. $w_j$ is the sprayed water density, which is calculated as follows:

$$w_j = \frac{Q_{s\,j}}{A_j} \quad (35)$$

where, $A_j$ is the sprayed area of the $j^{th}$ section and $Q_{sj}$ is the spray water flow rate in the $j^{th}$ section.

Radiation cooling region [16]:

$$q_n = h_{Ra}(T - T_{amb}) \quad (36)$$

$$h_{Ra} = \sigma\varepsilon(T^2 + T_{amb}^2)(T + T_{amb}) \quad (37)$$

where, $\varepsilon$ is the emissivity of the bloom surface (0.8), $\sigma$ is the Stefan–Boltzman constant *($5.67\times10^{-8}$ $W/m^2K^4$)*, and $T_{amb}$ is the ambient temperature *(K)*.

### 3-3- Microsegregation model

In order to calculate steel liquidus, solidus, and peritectic temperatures as well as phase fractions (as a function of temperature and chemical composition) required for the thermal analysis and strain analysis of solidifying steel, a non-equilibrium microsegregation model based on an analytical Clyne-Kurz style equation developed by Won and Thomas [17] is used. Liquidus, solidus, and peritectic temperatures depend on steel composition as follows:

$$T_{liq} = T_{pure} - \sum_i m_i\, C_{0,i} \quad (38)$$

$$T_{sol} = T_{pure} - \sum_i m_i\, C_{L,i}(C_{0,i}, k_i, D_i, CR, f_s = 1) \quad (39)$$

$$T_{start}^{\delta/\gamma} = T_{pure}^{\delta/\gamma} - \sum_i n_i\, k_i^{\delta/L}\, C_{L,i}^{\delta} \quad (40)$$

Extended data needed for this model are listed in Table 1 and include the partition coefficients ($k$) and diffusion coefficients ($D$) for each phase, as well as the slopes of the equilibrium liquidus ($m$) and the slopes of $Ar_4$ lines ($n$) for the pseudo-binary alloy of each element with iron.

*Table 1. Parameters required for the microsegregation model.*

| Element | $k^{\delta/L}$ | $k^{\gamma/L}$ | $D^{\delta}$ (cm2/sec) | $D^{\gamma}$ (cm2/sec) | $m$ (°C/%) | $n$ (°C/%) |
|---|---|---|---|---|---|---|
| C | 0.19 | 0.34 | 0.0127exp(-19450/RT) | 0.0761exp(-32160/RT) | 78.0 | -1122 |
| Si | 0.77 | 0.52 | 8.0exp(-59500/RT) | 0.3exp(-60100/RT) | 7.6 | 60 |
| Mn | 0.76 | 0.78 | 0.76exp(-53640/RT) | 0.055exp(-59600/RT) | 4.9 | -12 |
| P | 0.23 | 0.13 | 2.9exp(-55000/RT) | 0.01exp(-43700/RT) | 34.4 | 140 |
| S | 0.05 | 0.035 | 4.56exp(-51300/RT) | 2.4exp(-53400/RT) | 38.0 | 160 |

Note: R is gas constant of 1.987cal/mol K, and T is temperature in Kelvin.

## 4- Results and Validation

Table 2 shows the operational and solidification data required for the simulation of solidification during continuous casting of a bloom. To validate the present FPM-thermal analysis, the surface temperature of the bloom predicted by the present FPM was compared with both the surface temperatures predicted by FVM [15] and those measured by the thermography method.

*Table 2. The practical conditions and data used for the numerical simulation of bloom.*

| Parameter | Value |
|---|---|
| *mold dimensions*- m | 0.23 × 0.25 |
| *Mold length* - m | 0.78 |
| $V_C$ – m/min | 0.6 , 0.7 , 0.8 |
| *Mold level* - % | 85 |
| $Q$ – lit/min | 2347 |
| $T_{pouring}$ - °C | 1530 |
| $T_{sol}$ - °C | 1372 |
| $T_{liq}$ - °C | 1492 |
| $k_l$ - W/m k | 39 |
| $k_{st}$ - W/m k | $(21.6+8.35\times10^{-3}T)$ |
| $\rho_l$ – kg/m | $796598-0.619\times10^{-3}T$ |
| $\rho_{st}$ – kg/m | $(810591-0.5091\times10^{-3}T)$ |
| $C_l$ – J/kg K | 824.6157 |
| $C_{st}$ – J/kg K | $(429.849+0.1498\times10^{-3}T)$ |
| $\Delta T_w^T$ - °C | 4.9 |
| $\Delta H_m$ - J/kg | 2340000 |

Figure 3 compares the surface temperatures of the bloom simulated by FPM and FVM in various cooling regions. The same Figure shows the temperatures measured by the thermovision machine in the radiation cooling region. Due to the presence of a high concentration of water vapor in the spray cooling region, it was not easy to measure the surface temperature of the bloom in the spray cooling region by the thermography technique. The thermovision machine measures temperature on the basis of the wavelength raised at any temperature. In the first step, a piece of steel heated to 1000°C was used to calibrate the thermovision machine. Six points along the strand length of the bloom surface were measured so that each measured data is an average of six measurements.

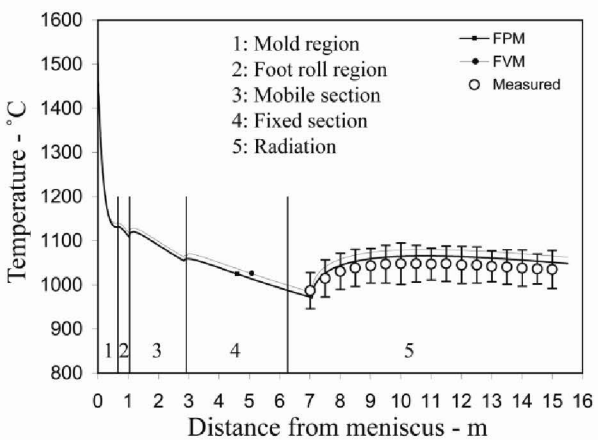


*Fig. 3. The surface temperature of bloom in different cooling zones simulated by FPM and FVM and also measured by the thermovision machine.*

It can be seen in Figure 3 that the profile of surface temperature simulated by FPM has a good agreement with that of the FVM. However, the temperature simulated by FVM is by almost 15-25°C higher than those of FPM. Comparison of the simulated results with the measured data shows that FPM data are closer to measured data than FVM results are. However, both FPM and FVM results lay within the range of standard deviations.

Figure 4 shows variations in surface and core temperatures of the bloom at the strand length for three different casting velocities. It is expected that increasing the casting velocity leads to increasing temperature profiles of the strand. This is due to the fact that increased casting speed causes the holding time of the bloom in the various cooling zones to be shortened. Figure 4 reveals this expected behavior predicted by FPM.

Another important investigation in a thermal analysis coupled with microsegregation calculations during continuous casting is the analysis of the mushy zone to study cracking. We, therefore, checked the calculation of the mushy zone in order to validate the proposed model. Figure 5 shows the positions of non-equilibrium solidus and liquidus

temperatures from chilled surface at the length of the strand simulated by both FPM and FVM. This Figure was plotted at $f_s = 1$ for the solidus temperature and at $f_s = 0$ for the liquidus temperature. As shown, the solidus and liquidus positions simulated by the proposed FPM are similar to the results obtained from FVM.

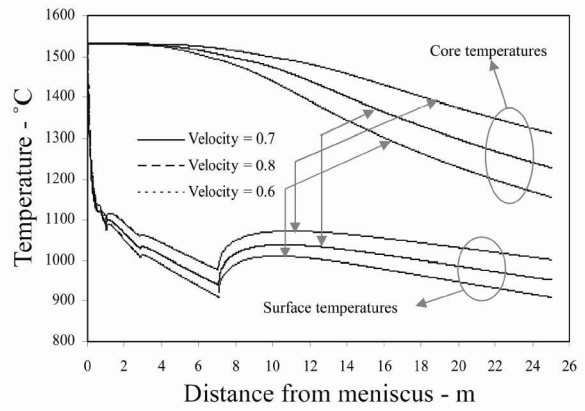


*Fig. 4. Variations of surface and core temperatures of the bloom at the strand length for three different casting velocities.*

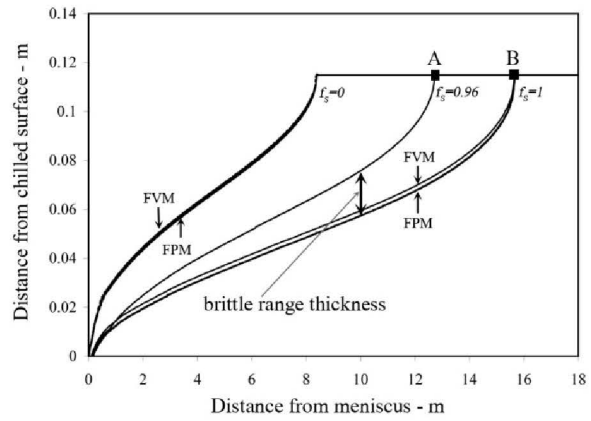


*Fig. 5. The positions of solidus and liquidus temperatures from chilled surface at the length of the strand simulated by both FPM and FVM.*

As already mentioned, a thermal model coupled with the microsegregation model is applied to calculate the requirements of hot tearing study; therefore, an instrumental thermal model should have enough flexibility to be easily coupled with the microsegregation model. In this subsection, the ability of the proposed model is investigated in determining hot tearing requirements.

During the continuous casting process, cracking strain only acts over a preferable range of the mushy zone. An important stage in hot tearing study is the determination of this preferable range known as brittle temperature range ($\Delta T_B$) which is limited between the solid fractions $f_S = 1$ and $f_S = 0.96$. Therefore, the following expression was stated for the brittle temperature range as the difference of temperatures corresponding to $f_S = 0.96$ and $f_S = 1$ [18]:

$$\Delta T_B = T(f_S = 0.96) - T(f_S = 1) \quad (41)$$

In fact, the term $\Delta T_B$ and the brittle range thickness are two important requirements for hot tearing study.

Figure 5 shows the brittle range of the mushy zone calculated by the proposed FPM-thermal analysis coupled with the microsegregation model. This region is limited between $f_S = 1$ and $f_S = 0.96$. As is clear from Figure 5, the line $f_S = 1$ comes to its end at a length of 15.8 m (point B) from meniscus and the line $f_S = 0.96$ ends at a length of 12.9 m (point A) from meniscus. The brittle range thickness is increased from meniscus up to point A after which it decreases by up to point B. Figure 6 shows the variation of brittle range thickness at the length of the strand for various casting speeds. The edge generated at a length of 6 m is due to the decrease in the cooling rate from the spray cooling zone to the radiation cooling zone. It can be seen that the brittle range thickness increased by up to a maximum value and then suddenly dropped to zero. This means that the tendency for hot tearing increases followed by a sharp decrease at the length of the strand. Fig. 6 also depicts the effect of casting speed on the behavior of brittle range thickness at the length of strand. According to this Figure, increasing casting speed has a considerable effect on the maximum position as well as on the end position of the diagram while the slope brittle range thickness follows a constant decreasing trend. Figure 6, plotted using the proposed FPM-thermal analysis coupled with the microsegregation model, reveals that the proposed model can be successfully used for cracking study.

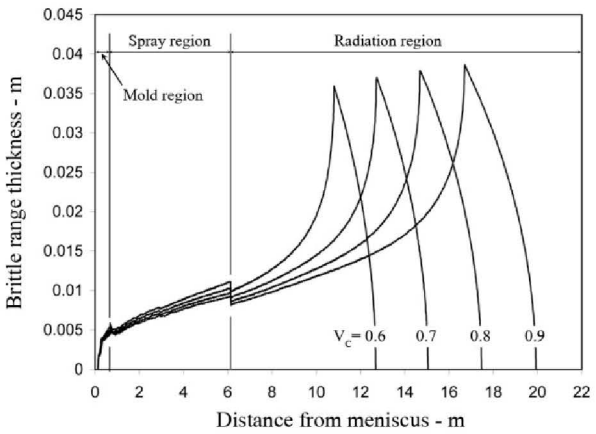


*Fig. 6. Variations in brittle range thickness at the length of strand for several casting speeds.*

Another requirement for hot tearing study which the proposed model is expected to calculate is the brittle temperature range. Figure 7 shows variations of $\Delta T_B$ at the length of strand for different casting speeds.

It has been demonstrated that increasing $\Delta T_B$ leads to a decrease in critical cracking strain resulting in increased crack susceptibility. It has also been found that increasing the casting speed and the

cooling rate causes the crack susceptibility to increase [18-20]. The results of Figure 7 confirm the above observations. It can be seen from Fig.7 that increasing the casting speed leads to increased $\Delta T_B$; i.e., increasing the casting speed increases crack susceptibility. Another finding illustrated in Figure 7 is that when the cooling rate decreases (from the Foot Roll area to the Radiation Area), a considerable decrease occurs in $\Delta T_B$ (from 65°C up to 47°C); this means that increasing cooling rate increases crack susceptibility.

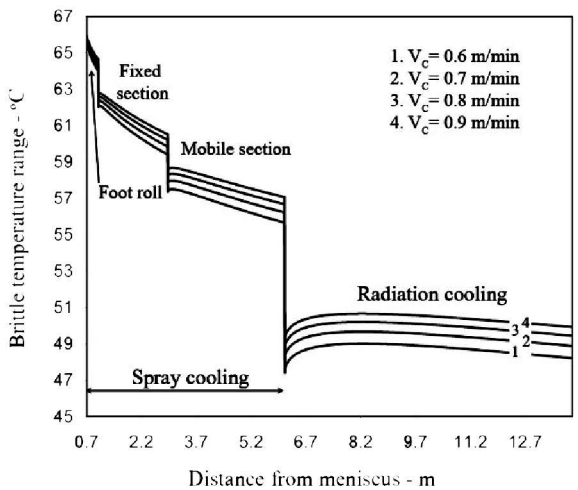


*Fig. 7. Variations of brittle temperature range at the length of strand for several casting speeds.*

## 5- Conclusion

To simulate the solidification process of a continuously cast bloom, a FPM was developed and the thermal analysis together with the microsegregation calculations of the bloom was carried out for various cooling regions. The results of thermal analysis such as solidus position, liquidus position, and temperature profiles of the core and surface simulated by FPM were compared with those obtained from FVM. The comparison shows a good agreement between the simulation resultsby both FPM and FVM. Also surface temperature measurements of the bloom in the radiation region validate the results from FPM and FVM. Also, the effect of casting speed on the thermal analysis was investigated to observe the same results as expected.

The results of microsegregation model coupled with the thermal model showed that the proposed model was able to analyze the mushy zone and that it could be useful in investigating the hot tearing phenomena during continuous casting.

Another finding of the present work was that the governing equations could be successfully converged using FPM coupled with microsegregation models for various casting speeds.

These observations indicate that FPM is a suitable method to simulate the continuous casting of steel in various cooling regions. An advantage of FPM found to be its accuracy and ease of application in the thermal analysis of continuous casting.

## 6- Acknowledgements

The authors would like to acknowledge the authorities of the Iran Alloy Steel Co. for their efforts in conducting plant experiments and for their financial support.

## References

[1] B. G. Thomas: ISS, Warrendale, PA, (2001), 3.
[2] N. Cheung and A. Garcia, Eng. Appl. Artif. Intel., 14 2001 , 229.
[3] H. Wang, G. Li, Y. Lei, Y. Zhao, Q. Dai and J. Wang, ISIJ Int., 45 (2005), 1291
[4] Toshihiko Emi, The Making Shaping and Treating of Steel-Casting, ed. A. W. Cramb (AISE Steel Foundation, Pittsburgh, 11th Edition, (2003), 2.
[5] S. Qiu, H. Liu, S. Peng and Y. Gan, ISIJ Int., 44 (2004), 1376
[6] H. Yang, L. Zhao, X. Zhang, K. Deng, W. Li and Y. Gan, Metall. Mater. Trans. B, 29 (1998), 1345.
[7] J. Konishi, M. Militzer, J. K. Brimacombe and I. V. Samarasekera, Metall. Mater. Trans. B, 33 (2002), 413.
[8] M. M. Hamdi, H. Combeau and G. Lesoult, Int. J. Numer. Method. H., 9 (1999), 296.
[9] Gui R. Liu: Mesh Free Methods, CRC, New York, (2003), 19.
[10] T. Belytschko, Y. Krongauz, D. Organ, M. Fleming and P. Krysl, Comput. Method. Appl. M., 139 (1996), 3.
[11] E. Onate, S. Idelsohn, O. C. Zienkiewicz, R. L. Taylor and C. Sacco, Comput. Method. Appl. M., 139 (1996), 315.
[12] E. Onate, S. Idelsohn, O. C. Zienkiewics and R. L. Taylor, Int. J. Numer. Method. Eng., 39 (1996), 3839.
[13] L. Zhang, Y. M. Rong, H. F. Shen and T. Y. Huang, J. Mater. Proc. Tech., 192- 193 (2007), 511.
[14] S. Louhenkilpi, J. Miettinen, L. Holappa, ISIJ Int. 46 (2006), 914.
[15] M. Alizadeh, A.J. Jahromi and O. Abouali, Comput. Mater. Sci., 44 (2008), 807.
[16] R. A. Hardin, K. Liu, A. Kapoor and C. Beckermann, Metall. Mater. Trans. B, 34(2003), 297.
[17] Y. Won, B. G. Thomas, Metall. Mater. Trans. A, 32 (200l) , 1755.
[18] C. Bernhard, R. Pierer, C. Chimani, Proc. of 5th Decennial Int. Conf. on Solification Processing, Sheffield, UK, (2007), 525.
[19] C. Bernhard, R. Pierer, A. Tubikanec, C. Chimani, Proc. of the CCR'04 – Continuous Casting and Hot Rolling Conference, Linz, Austria, (2004) 6.3.
[20] Y. M. Won, H. N. Han, T. Yeo, K. H. Oh, ISIJ Int., 40 2000 , 129.